

Large-image-format computed tomography imaging spectrometer for fluorescence microscopy

Bridget K. Ford and Michael R. Descour

University of Arizona, Optical Sciences Center, Tucson, Arizona 85721 USA
bford@u.arizona.edu, michael.Descour@optics.arizona.edu

Ronald M. Lynch

University of Arizona, Department of Physiology, Tucson, Arizona 85721 USA
rlynch@u.arizona.edu

Abstract: Multispectral imaging has significantly enhanced the analysis of fixed specimens in pathology and cytogenetics. However, application of this technology to *in vivo* studies has been limited. This is due in part to the increased temporal resolution required to analyze changes in cellular function. Here we present a non-scanning instrument that simultaneously acquires full spectral information (460 nm to 740 nm) from every pixel within its 2-D field of view (200 μm x 200 μm) during a single integration time (typically, 2 seconds). The current spatial and spectral sampling intervals of the spectrometer are 0.985 μm and 5 nm, respectively. These properties allow for the analysis of physiological responses within living biological specimens.

©2001 Optical Society of America

OCIS codes: (180.2520) Fluorescence Microscopy; (300.6190) Spectrometers

References and Links

1. W. T. Mason, ed. *Fluorescent and Luminescent Probes for Biological Activity: A Practical Guide for Quantitative Real-Time Analysis*. (Academic Press, 1999).
2. R. Haugland, *Handbook of fluorescent probes and research chemicals. Eighth Edition*. (Molecular Probes, Inc., 2001).
3. R. M. Lynch, K. D. Nullmeyer, B. K. Ford, L. S. Tompkins, V. L. Sutherland and M. R. Descour, "Multi-parametric analysis of cellular and subcellular function by spectral imaging," in *Molecular Imaging: Reporters, Dyes, Markers and Instrumentation*, D. J. Burnhop and K. Licha, eds., Proc. SPIE **3924**, 79-87 (2000).
4. K. N. Richmond, S. Burnite and R. M. Lynch, "Oxygen sensitivity of mitochondrial metabolic state in isolated skeletal and cardiac myocytes," *Am. J. Physiol.* **273 (Cell 42)**, C1613- C1622 (1997).
5. R. Martinez-Zaguilan, M. Gurule and R. M. Lynch, "Simultaneous Measurement of pH and Ca^{2+} in single insulin secreting cells by microscopic spectral imaging," *Am. J. Physiol.* **270 (Cell 40)**, C1438-1446 (1996).
6. R. Martinez-Zaguilan, L. S. Tompkins, R. J. Gillies and R. M. Lynch, "Simultaneous measurements of calcium and pH in cell populations," in *Calcium Signaling Protocols, Meth. Molec. Biol. Series*, Vol. 114, D.G. Lambert, ed. (Humana Press, 1999), Chap. 20.
7. E. Schröck, S. du Manoir, T. Veldman, B. Schoell, J. Wienberg, M. A. Ferguson-Smith, Y. Ning, D. H. Ledbetter, I. Am-Bar, D. Soenksen, Y. Garini, T. Ried, "Multicolor spectral karyotyping of human chromosomes," *Science* **273**, 494-497 (1996).
8. E. S. Wachman, W. Niu and D. L. Farkas, "AOTF microscope for imaging with increased speed and versatility," *Biophys J.* **73**, 1215-1222 (1997).
9. H. R. Morris, Hoyt C. C., Treado P. J., "Imaging spectrometers for fluorescence and Raman microscopy—acoustooptic and liquid-crystal tunable filters," *Appl. Spectrosc.* **48**:857-866
10. N. M. Haralampus-Grynawski, M. J. Stimson, and J. D. Simon, "Design and Applications of Rapid-Scan Spectrally Resolved Fluorescence Microscopy," *Appl. Spectrosc.* **54**, 1727-1733 (2000)
11. M.E. Dickinson, "Spectral imaging with multiphoton excitation microscopy," in *Imaging Life: From cells to whole animals*. Microscopy and Microanalysis Pre-Meeting Congress, Long Beach California (2001).

12. C. E. Volin, B. K. Ford, M. R. Descour, J. P. Garcia, P. D. Maker, G. H. Bearman, "High-speed spectral imager for imaging transient fluorescence phenomena," *Appl. Opt.* **37**, 8112–8119 (1998).
13. B. K. Ford, S. M. Murphy, C. E. Volin, R. M. Lynch, and M. R. Descour, "Computed-Tomography based video-rate spectral imaging system for fluorescence microscopy," *Biophys. J.* **80**, 986-993 (2001).
14. S. A. Clark, B. L. Burnham, and W. L. Chick, "Modulation of glucose-induced insulin secretion from a rat clonal β -cell line," *Endocrinology*, **127**(6), 2779-2788 (1990).
15. B. K. Ford, C. E. Volin, A. R. Rouse, R. M. Lynch, A. F. Gmitro, G. H. Bearman and M. R. Descour, "Video-rate spectral imaging system for fluorescence microscopy," in *Systems and Technologies for Clinical Diagnostics and Drug Discovery II*, G. E. Cohn, ed., Proc. SPIE **3603**, 3603-3629 (1999).
16. Olympus America, Inc. Melville NY, 11747, <http://www.olympus.com>.
17. DALSA Tucson, Tucson, AZ 85713, <http://www.dalsa.com>.
18. Jet Propulsion Laboratory, Pasadena, CA 91109.
19. Volin, C. E, *Portable snapshot infrared imaging spectrometer*, Ph.D. Dissertation, University of Arizona. (2001).
20. M. R. Descour, C. E. Volin, T. M. Gleeson, E. L. Dereniak, M. F. Hopkins, D. W. Wilson and P. D. Maker, "Demonstration of a Computed-Tomography Imaging Spectrometer using a computer-generated hologram disperser," *Appl. Opt.* **36**, 3694-98 (1997).
21. M. R. Descour and E. Dereniak, "Computed-tomography imaging spectrometer: Experimental calibration and reconstruction results," *Appl. Opt.* **34**, 4817-4826 (1995).
22. M. R. Descour, C. E. Volin, E. L. Dereniak, K. J. Thome, A. B. Schumacher, D. W. Wilson and P. D. Maker, "Demonstration of a High Speed Non-scanning Imaging Spectrometer," *Opt. Lett.* **22**, 1271-1273 (1997).
23. J. D. Gaskill, *Linear Systems, Fourier Transforms, and Optics* (John Wiley and Sons, Inc, 1978) Chap. 5.
24. A. Lent, "A convergent algorithm for maximum entropy image restoration," in *Image Analysis and Evaluation*, Rodney Shaw, ed. SPSE Proceedings, 249-257 (1976).
25. Ocean Optics, Inc. Dunedin, FL 34698, <http://www.oceanoptics.com/homepage.asp>.
26. R. M. Lynch, K. E. Fogarty and F. S. Fay, "Analysis of hexokinase association with mitochondria by quantitative confocal microscopy," *J. Cell Biol.* **112**, 385-395 (1991).
27. M. P. Bruchez Jr., M. Moronne, P. Gin, S. Weiss, A. P. Alivisatos, "Semiconductor nanocrystals as fluorescent biological labels, *Science* **281**, 2013-2016 (1998).

1. Introduction

Fluorescent molecules are commonly utilized to monitor changes in cellular morphology, ion and metabolite concentrations and gene expression. Examination of these parameters yields valuable insight into the underlying mechanisms associated with basic cellular responses [1,2]. However, scanning requirements of existing spectrometers may limit investigations into the fundamental processes involved in more complicated signaling cascades. Such experiments require the use of a spectral imaging system that collects high-resolution spectral data simultaneously for all spatial locations across the cellular field [3]. This can be appreciated by noting that several cellular parameters may change either simultaneously or in sequence during the course of many physical responses (e.g. hormone secretion, muscle contraction) [4,5]. Since many tissues are heterogeneous with respect to the time course of cellular response, it is critical to examine multiple parameters in individual cells with adequate spatial (1 μm or less) and temporal resolution (msec – sec). Such observations of multiple physiological parameters require the loading of several distinct probes into the cellular environment. These probes may exhibit overlapping spectral signatures, dye-dye interactions or cross-sensitivities to multiple analytes. Under these circumstances, spectral unmixing algorithms can be utilized to precisely evaluate the signal from individual probes and to evaluate possible spectral variations due to probe interactions [6,7]. Thus, in addition to high spatial and temporal sampling, data must be collected with high spectral resolution over a continuous spectral range.

With currently available imaging spectrometers, the need for scanning results in an often-unacceptable compromise between spectral, spatial and temporal resolution. For instance, due to the need for spectral-band scanning in filtered imaging systems, an improvement in spectral resolution occurs with a concomitant reduction in temporal resolution [8,9]. Such a tradeoff results either from restrictions on the system's scan rate or from a reduction in the

signal to noise ratio within the narrow spectral bandwidth of each filtered image. An example of a filtered imaging system currently used in fluorescence microscopy is a camera equipped with either an acousto-optic tunable filter (AOTF) or liquid crystal tunable filter (LCTF). Although these devices exhibit rapid switching rates between spectral bands, the signal within each band ultimately limits their temporal resolution. The lengthy acquisition times result in a significant temporal offset between the signals detected from different physiological markers and therefore ambiguity in determining the time course of physical response.

Point-scan and slit-scan spectrometers overcome this drawback by collecting high-resolution spectral data over a limited region of the cellular field [10,11]. Yet, due to cellular heterogeneity within a sample it is important to observe the interactions of multiple cell types and therefore some form of spatial scanning is required. Again, the scan rates of these systems are not the limiting factor in determining their temporal resolution. Instead one must consider the dwell time required at each point or line within the sample. Thus the practical limit on the temporal resolution of these systems is the available fluorescence signal and the instrument's detection efficiency. In a recent publication, a total acquisition time of less than 5 minutes has been reported for acquiring an object cube (200 x 200 spatial positions, 0.4 nm spectral sampling) using a slit scan imaging spectrometer in fluorescence microscopy [10]. Since changes in the sample may occur during the scanning process, the exact time sequence of events across the scanned field becomes difficult to verify.

The instrument described in this paper overcomes previous limitations by acquiring full spectral information for all points within a 2-D field of view (FOV) during a single integration time. For this reason, the computed tomography imaging spectrometer (CTIS) can be considered a snapshot spectral imaging device. The design and application of a first-generation system was presented previously [12,13]. The instrument used during these exploratory studies was originally developed for remote sensing purposes and therefore lacked both the field of view and optimal noise characteristics required for biological applications. However, using this prototype, we were able to demonstrate the applicability of the CTIS to standard physiological experiments. Specifically, we were able to follow the response of SNARF-1, a fluorescent probe, to changes in pH in an insulin secreting rat insulinoma cell line RIN-38 [13,14].

In this paper we present preliminary spectral imaging results from a large format CTIS and also provide a description of this second-generation system's design and imaging capabilities.

2. Instrumentation

The CTIS is a modular instrument that can be coupled to a wide variety of imaging systems. In the context of fluorescence microscopy, the interchangeable fore-optics include fluorescence microscopes and imaging endoscopes [15]. For the purposes of this paper, the fore-optics consist of a commercially available inverted fluorescence microscope from Olympus, Inc (Olympus IX70) [16]. An image of the complete system is provided in Figure 1. To generate the images presented here, the samples were illuminated using a 250 W Xenon arc lamp. A 10 nm bandpass filter was used to select a narrow excitation range centered at 490 nm. The fluorescence emission was collected by a 40x, 1.35 NA microscope objective. This optic was followed by a 505 nm dichroic beamsplitter and a 515 nm long-pass emission filter such that light emitted from the fluorophores was passed on to the CTIS while the excitation light was suppressed. An intermediate image was then formed outside the side photo port of the microscope at the field stop of the CTIS.

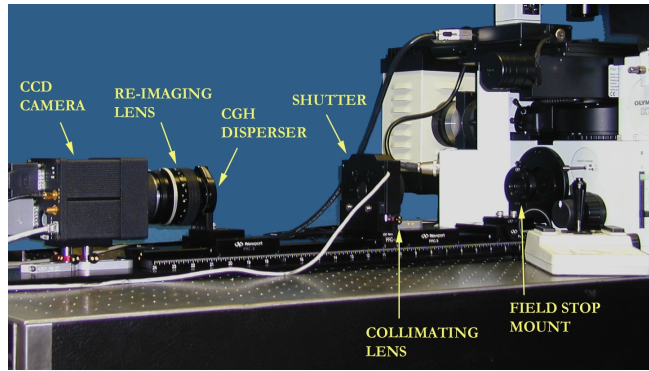


Fig. 1. Digital image of the large-format CTIS aligned to the side photo port of an Olympus IX70 inverted fluorescence microscope.

The optical train of the CTIS includes the field stop, collimator and re-imaging lenses, computer-generated-hologram (CGH) disperser and CCD detector array (Dalsa, 4M4) [17]. The DALSA 4M4 is a 12-bit, cooled digital scientific camera with 2048×2048 pixels ($14 \mu\text{m}$). The CCD has a maximum quantum efficiency of $\sim 38\%$ at 750 nm and a dark current rate of $300 \text{ electrons/pixels/sec}$ at 25°C . The quantum efficiency and dark current rate represent significant improvements over previous CTIS prototypes [12,13]. The CTIS is constructed with commercial optics, with the exception of the CGH disperser. The disperser is designed to produce a 5×5 array of diffraction orders on the CCD array. The surface relief of the CTIS CGH disperser is generated by using electron-beam lithography in a film of polymethylmethacrylate (PMMA) on a fused silica window (Jet Propulsion Lab, CA) [18]. The CGH disperser consists of an array of identical square unit cells. Each unit cell is subdivided into an integral number of square pixels. The physical depths assigned to the pixels provide the necessary phase delays that in turn result in the desired diffraction pattern. In the case of the large format CTIS, the 17 mm -diameter CGH disperser consists of $12 \mu\text{m} \times 12 \mu\text{m}$ unit cells that are each composed of an 8×8 array of $1.5 \mu\text{m}$ pixels [19]. An optical microscope image of a section of the CGH disperser's surface is provided in Figure 2.



Fig. 2. Optical microscope image of a segment of the CGH disperser (Courtesy of D. W. Wilson and P. D. Maker, Jet Propulsion Laboratory).

The CGH disperser is designed so that a maximum fraction of the light collected by the microscope objective contributes to the raw image. Specifically, light is suppressed in the disperser's higher diffraction orders while the sum of diffraction efficiencies (η_{tot}) is maximized within the central 25 orders comprising the raw image (Figure 5). Measurements of η_{tot} have been as high as 78% [20]. In order to maintain the same signal and thus the same signal-to-noise ratio across the raw image, the disperser is designed so that the

diffraction efficiency $\eta(\lambda)$ increases in higher diffraction orders to compensate for the increasing dispersion.

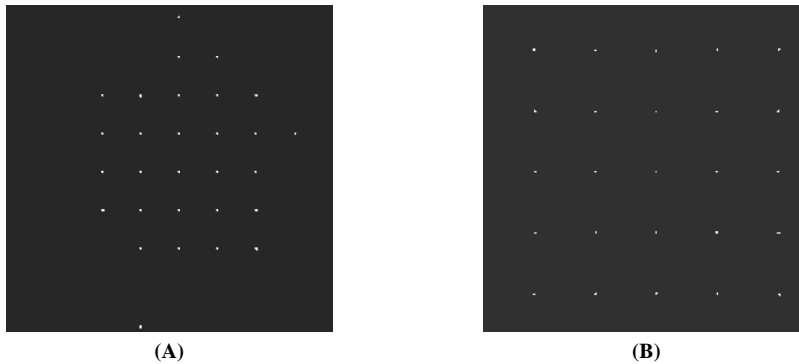


Fig. 3. Mapping of the signal from individual voxels to the imaging array. The signal on the imaging array is distributed in a diffraction pattern that depends on a voxel's (x, y, λ) coordinates in the object cube. Calibration images are shown for two different voxels that occupy the same spatial position but different spectral bands. Part (a) corresponds to a voxel with a center wavelength of 470 nm while Part (b) corresponds to a center wavelength of 740 nm.

In modeling the function of the CTIS, the continuous 3-D (x, y, λ) object cube is interpreted as a collection of smaller, contiguous volume elements, i.e., voxels $(\Delta x, \Delta y, \Delta \lambda)$. The CTIS maps the signal from each voxel to a distinct diffraction pattern on a CCD array by means of the CGH disperser. In forming the raw image, a set of diffraction patterns, such as the two examples shown in Figure 3, is recorded for all voxels in the object cube during a single integration time. A shift in the center wavelength of a voxel results in the expansion or contraction of the diffraction pattern within the CTIS image plane. A change in the voxel's spatial position results in a corresponding translation of the diffraction pattern across this image plane. The ensemble of the diffraction patterns associated with all voxels represents the mapping from the 3-D (x, y, λ) object space to the 2-D image space (CCD detector array) effected by the CTIS (Figure 4). This mapping can be mathematically inverted to reconstruct an object cube from a raw image (see Section 3).

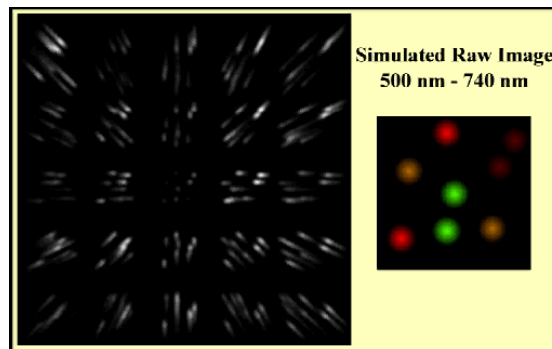


Fig. 4. (821 KB) Movie demonstrating how the CTIS maps a 3-D (x, y, λ) object cube onto a 2-D image plane. The sequence corresponds to simulated raw images of the same specimen viewed through a filter of increasing spectral bandwidth. The movie begins with a narrow-band image (500 nm - 510 nm). The bandwidth increases in steps of 10 nm to a maximum of 240 nm (500 nm - 740 nm). The simulated object cube consists of eight spheres with four different emission maxima (530 nm, 515 nm, 560 nm, 615 nm).

The zeroth diffraction order image is located at the center of the raw image (see Figures 4 and 5) and is the result of direct imaging through the CGH disperser without any dispersion. This image therefore represents an undispersed, broadband view of the specimen. Consequently, the zeroth diffraction order image can be used to aim and focus the microscope without the need for any data processing. Thus, sample selection and initial positioning information are easily obtained. The higher order images are associated with an increasing dispersion that manifests itself as a radial blur in the higher diffraction orders (Figure 5).

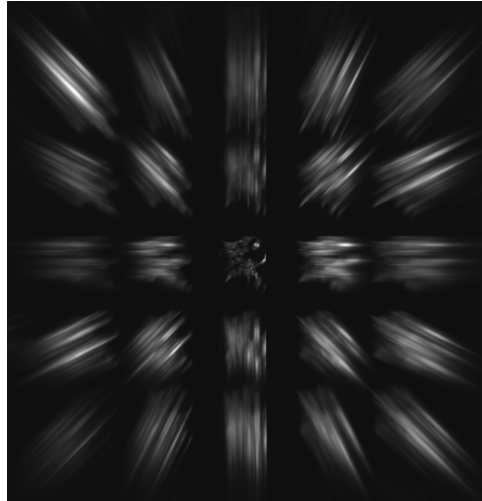


Fig. 5. Representative raw image of embryonic rat cerebellum glia. The cells were probed with primary antibodies to glial fibrillary acidic proteins (GFAP) and subsequently labeled with Alexa Fluor 488 goat anti-rabbit IgG (H+L) conjugate secondary antibody and the DNA/RNA probe, Ethidium Bromide. The image was taken using a 40x, NA = 1.35 microscope objective. Object cubes were reconstructed with 55 spectral bands (470nm – 740 nm, spectral sampling distance of 5 nm) and 203 x 203 spatial resolution elements. The spatial sampling distance between adjacent pixels is 0.985 μm for this application

3. Reconstruction Algorithm

The CTIS instrument is modeled as a linear imaging system and therefore may be described in terms of linear algebra. The 2-D image (Figure 5) and the 3-D object cube are re-organized as vectors \mathbf{g} and \mathbf{f} , respectively. These vectors are related to each other by means of a system matrix, denoted by H . Each column of H corresponds to the response of the CTIS to a single voxel ($\Delta x, \Delta y, \Delta \lambda$) in the object cube. The matrix H can be acquired experimentally by recording calibration images, such as those shown in Figure 3, for every voxel within the object cube [19,21,22]. In order to obtain the raw image associated with a single voxel, light from a 100W Tungsten-Halogen lamp is focused onto the entrance slit of a monochromator. The narrow-bandwidth light emerging from the monochromator is coupled into an optical fiber and the output of this fiber is focused to a spot in the field stop of the CTIS. Ideally, the size of this spot is such that only a single detector element on the CCD array is illuminated within the 0th diffraction order image of the spot. Deviations from this ideal situation occur due to the inherent axial chromatic aberration of the optics focusing the monochromator's output. After the set of calibration images are acquired, the output of the fiber is focused onto a spectrally calibrated radiometer and is scanned through wavelength. A product is formed at each wavelength between the radiometer's output (measured in mW) and the integration time required for the calibration image. This product serves as a normalization factor for each column of the H matrix so that the reconstructed datacube is in units of $\mu\text{J}/\text{spectral band}$. For a more detailed description of the calibration process see Refs. 19 and 21.

As a result of the spatial shift-invariance of the CTIS instrument, only a single calibration image per wavelength band needs to be acquired and stored [12,23]. During reconstruction of the object cube, these stored calibration images are recalled and shifted to the required spatial position within the field of view.

The reconstruction of the 3-D object cube is performed using the Multiplicative Algebraic Reconstruction Technique (MART). The iterative progression from the k^{th} estimated object cube, $\hat{\mathbf{f}}^k$, to the $(k + 1)^{\text{st}}$ occurs according to the equation:

$$\hat{\mathbf{f}}^{k+1} = \hat{\mathbf{f}}^k \frac{H^T \mathbf{g}}{H^T H \hat{\mathbf{f}}^k}, \quad (1)$$

where T indicates the matrix transpose and $H^T \mathbf{g}$ and $H^T H \hat{\mathbf{f}}^k$ form the backprojection of the collected raw image and the current image estimate, respectively. The multiplications and divisions are taken to be element-by-element operations [24].

Reconstruction tests performed in conjunction with a non-imaging reference spectrometer are used to determine the number of iterations of MART that yield the highest accuracy in the reconstructed spectra. In our experiments, seven or eight iterations typically prove optimal. In practical imaging situations in which noise corrupts the raw image, an additional increase in the number of iterations does not result in higher reconstruction accuracy. Instead, noise artifacts begin to dominate the reconstructed spectra of each pixel. These noise artifacts tend to take the form of nonphysical discontinuities between adjacent spectral bands.

The results presented in the next section were obtained after eight iterations of the reconstruction algorithm in Equation 1. Individual iterations required approximately 6 minutes to complete using a 1 GHz Pentium III personal computer to reconstruct 203×203 spatial resolution elements and 55 spectral bands. In our current work, the initial estimate of the object cube, $\hat{\mathbf{f}}^0$, corresponds spatially to the zeroth-order image and is spectrally uniform.

4. Microsphere imaging experiments

4.1 Sample preparation

A sample containing a mixture of polystyrene microspheres with four different emission maxima (Molecular Probes F-8833, F-8834, F-8836) was prepared by depositing $10 \mu\text{l}$ of diluted stock suspension onto a glass microscope slide. The solution was allowed to air-dry and was then covered by a small drop of mounting medium (Molecular Probes M-7901). A coverslip was placed on the slide and sealed with clear nail enamel.

4.2 Imaging results

A mixture of $10 \mu\text{m}$ -diameter microspheres with different fluoresce characteristics was imaged through the microscope and the large-image-format CTIS. Due to the relatively large fluorescence signal associated with the microspheres, a high degree of temporal resolution also was realized. Raw images were recorded using a 12-bit digital scientific camera and an integration time of 50 ms. Figure 6 shows a post reconstruction image for this sample. Object cubes were reconstructed with 55 spectral bands (spectral sampling interval of 5 nm) and 203×203 spatial resolution elements. Reconstructed spectra from three different spatial positions are shown in Figure 7. The crosses denote spectra measured for comparison with a radiometrically-calibrated non-imaging spectrometer (Ocean Optics, Inc. Model S2000) [25]. These results demonstrate the potential capability of the large-image-format CTIS to simultaneously capture accurate spectral signatures of multiple fluorophores from different regions within the same sample with a relatively high temporal resolution.

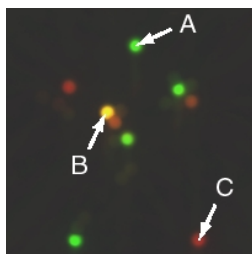


Fig. 6. Reconstructed image of a mixture of microspheres with different emission spectra. Color image is generated by converting the reconstructed spectra into sets of RGB values.

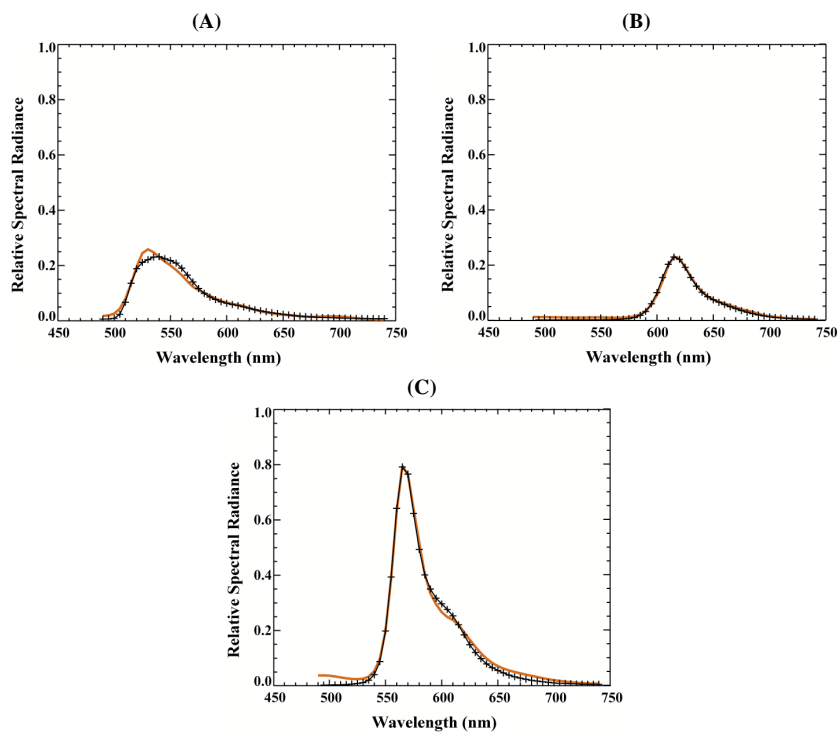


Fig. 7. Reconstructed spectra corresponding to three different locations within the microsphere sample. See Fig. 6 for locations (A), (B) and (C). Crosses denote comparison spectra measured with a radiometrically calibrated non-imaging spectrometer.

5. Cellular imaging experiments

5.1 Sample preparation

Glial cells were isolated from embryonic rat cerebellum and grown in cell culture. Glia grown on glass coverslips were fixed by incubation in a 4% Paraformaldehyde solution (for details see Ref. 26). The primary antibody labeling of GFAP was carried out by incubating the cells for 45 minutes at room temperature in a solution of rabbit anti-Glial fibrillary acidic protein (GFAP) (Sigma G-9269). The cells were then incubated at room temperature for 45 minutes in a solution of a 1:100 dilution of Alexa Fluor 488 goat anti-rabbit IgG (H+L) conjugate (Molecular Probes A-11008, 2 mg/ml) and 2:1000 dilution of 10 mg/ml Ethidium Bromide (Sigma E-8751).

5.2 Imaging results

The raw image shown in Figure 5 was recorded using a digital scientific camera with an integration time of 2.5 seconds. Object cubes were again reconstructed with 55 spectral bands (spectral sampling interval of 5 nm) and 203 x 203 spatial resolution elements. Figure 8 shows the post-reconstruction image with two marked pixel locations. These correspond to the reconstructed spectra in Figure 9.

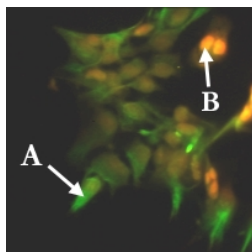


Fig. 8. Color image reconstructed from the raw image shown in Figure 5. Green fluorescence indicates the distribution of GFAP while orange-red indicates nucleic acid distribution.

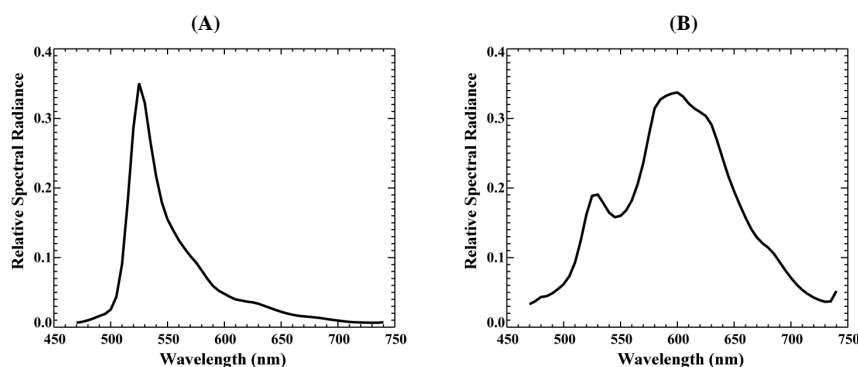


Fig. 9. Reconstructed spectra of two pixel locations within the reconstructed image of Figure 8. The locations (A) and (B) are indicated in Figure 8.

6. Summary

The response of biological systems to changes in the cellular environment is often a complex cascade of intracellular signaling events. These events may include changes in the concentration of ions and metabolites, levels of gene expression or even modifications to the cellular morphology. Moreover, these changes may be unique to individual cells within a given population. Examples include cells within a tissue such as a liver slice or a population of isolated cells such as neuronal cultures. To understand how individual cells respond and how interactions between unique cell types occur, it is critical to simultaneously monitor multiple functional parameters from many cells. The ability to simultaneously monitor several underlying factors with high temporal and spatial resolution will enhance our ability to understand these complex-signaling processes.

In the present work, we have demonstrated the imaging capabilities of a large-image-format CTIS designed for multispectral imaging of fluorescently labeled biological specimens. Compared to previous versions, the large-image-format CTIS described here represents a six-fold increase in the number of spatial resolution elements across the instrument's FOV, which now consists of 203 x 203 pixels. This increase was a result of a larger detector format and a redesigned optical system. This included reducing the number of

diffraction orders in the raw image from 49 to 25 in order to accommodate the larger 0th order image and to maintain minimum overlap between the dispersed images.

The spatial resolution of the system is dependent upon the microscope objective used. In this paper we presented results using a 40x, NA=1.35 that yields a spatial sampling distance of 0.985 μm and a FOV of 200 μm x 200 μm . We have also reduced our spectral sampling interval from 10 nm to 5 nm to allow for improved differentiation of spectrally similar fluorophores. The spectral resolution achieved in reconstructed object cubes is dependent upon the spectral sampling between adjacent calibration images and therefore can be adjusted to fit the experimental requirements. These characteristics provide the spatial and spectral resolution required to analyze the response of several fluorescent probes within individual cells.

The temporal resolution of the CTIS is ultimately limited by the readout rate of the CCD detector (20MHz in the case of the DALSA 4M4 camera). In practice, however, the temporal resolution is actually limited by the integration time required to record the low signal levels, typical of fluorescent probes loaded within the cellular environment. Therefore, the CTIS now employs a CCD detector array with a higher quantum efficiency (maximum value \approx 38% at 750 nm, minimum value \approx 10% at 470 nm) and a reduced dark current rate (300 electrons/pixel/sec at an operating temperature of 25°C). For analysis of typical biological specimens, integration times of 1-2 seconds are currently required. The full spatial and spectral information required to reconstruct an object cube is acquired during this single integration time. In the case of fluorescing microspheres, the temporal resolution (integration times of 50 ms) is greatly enhanced due to the relatively high fluorescent yield. Integration times for biological specimens could approach 1 second or less by replacing the current detector with one of higher quantum efficiency ($>$ 80%). In addition, with the development of large-format intensified-CCD detectors, the possibility for near real-time spectral imaging is limited only by the detector's readout rate.

A limitation on the usefulness of the CTIS is one associated with the entire field of multispectral imaging in biology. In order to simultaneously monitor multiple physiological parameters, certain characteristics are required of the fluorescent probes. Specifically, the probes should all excite below and emit above the cut off of the microscope dichroic filter such that a single filter set can be used to collect the full emission spectrum. In addition, the probes must exhibit a range of desired specificities. Combinations of probes with these characteristics do exist but are limited. With the ongoing development of new functional probes including nanocrystals with specific affinities to physiological parameters, this restriction may also be overcome [27]. With these technological improvements, the CTIS is a suitable instrument for studying changes in multiple physiological parameters across a heterogeneous cell population with practical spatial, spectral and temporal resolutions.

In all, the ability of the CTIS to simultaneously acquire data over a broad spectral range at precise spatial positions offers several benefits over existing spectral-imaging microscopy systems. These benefits include spatial co-registration of spectral images and the possibility of high temporal resolution when the CTIS is coupled to a camera with a fast read-out rate. The temporal sampling rate of the CTIS is limited only by the detector read-out rate and the signal-to-noise ratio on the array, which currently falls within the range required for many physiological experiments (0.01-2 sec).

Acknowledgements

The authors wish to thank E. L. Dereniak of the Optical Sciences Center and Marguerite Green of the University of Arizona Department of Physiology for their support of and assistance with the work presented in this paper. We are also grateful to D. W. Wilson and P. D. Maker of the Jet Propulsion Laboratory for the fabrication and testing of the CGH disperser. This material is based upon work supported by the National Science Foundation under Grant No. 9876717 (MRD and RML) and the American Diabetes Association (RML).